Trans. JSASS Aerospace Tech. Japan
Vol. 12, No. ists29, pp. Pb_13-Pb_18, 2014

Original Paper

Investigation of Plasma Characteristics and Ion Beam Extraction for a Micro RF Ion Thruster

By Yoshinori TAKAO, Masataka SAKAMOTO, Koji ERIGUCHI and Kouichi ONO

Department of Aeronautics and Astronautics, Kyoto University, Kyoto, Japan

(Received June 28th, 2013)

Two-dimensional axisymmetric particle-in-cell simulations with a Monte Carlo collision algorithm, external circuit analysis, and measurements of plasma densities and ion beam currents have been conducted for a micro RF ion thruster. The plasma source of the thruster is 5.0 mm in radius and 10 mm in length with a five-turn helical coil around a cylindrical quartz chamber, where the plasma is generated at low RF powers (< 10 W). The numerical results have indicated that high RF frequencies (> 100 MHz) lead to a high coupling efficiency between the RF power and the plasma, although too high RF frequencies (> 300 MHz) degrade the efficiency. The optimum gas flow rate for ion beam extraction is determined to be 10 μg/s. These results are qualitatively in good agreement with the experimental results, which validates our numerical model, and thus the model would be useful to estimate the performance of the micro RF ion thruster.

Key Words: Micro Ion Thruster, RF Plasma, PIC-MCC, Circuit Model, Ion Beam Extraction

Nomenclature

C	:	capacitance
f	:	RF frequency
I	:	current
L	:	self-inductance
M	:	mutual inductance
n	:	number density
p	:	pressure
P	:	power
R	:	resistance
V	:	voltage
ν_{me}	:	momentum transfer collision frequency between electrons and neutrals
ρ	:	plasma resistance
ϕ	:	potential
χ	:	plasma reactance
ω	:	angular frequency

Subscripts

abs	:	absorption
b	:	beam
cap	:	capacitive
e	:	electron
g	:	RF generator
in	:	input
ind	:	inductive

1. Introduction

In recent years, because of low development and launch costs and short development periods of microspacecraft, the worldwide interest in microspacecraft has grown to such an extent that even universities are currently able to launch and operate microspacecraft. However, most microspacecraft that universities operate do not have any propulsion systems, which is why they rely on passive controls, such as gravity gradient stabilization, and geomagnetic attitude stabilization. If a microspacecraft had microthrusters mounted on it, we could control the microspacecraft more effectively to create a specific flight path. Owing to the limited power generation and propellant storage, high specific impulses, high-thrust efficiencies, and low-power consumptions are required for microthrusters, in addition to small size and light weight [1]. Several types of microthrusters are proposed and some of them are already developed. Among them, ion thrusters are one of the most promising propulsion systems for microspacecraft.

In order to develop such a micro ion thruster, we have to figure out how to generate plasma in a small space and how to extract ions from it efficiently and effectively. A lot of experimental studies have already been carried out. However, the information obtained from such experiments is always limited because of the small size. The spatial distribution of plasma parameters in small space less than a centimeter is not readily available in experiments. This is why numerical simulations can also be useful to compensate for lack of information, and the combination of experimental and numerical studies would be important. To develop a reasonable numerical model, simplicity is a key factor. The micro RF ion thruster presented in this study is one of the simplest ion thrusters as shown in Fig. 1. The thruster consists of a cylindrical micro inductively coupled plasma source (ICP), which has no magnets or cathodes, and a grid system with a single hole on the central axis. Because of this structure, the ion thruster can be modeled in the two-dimensional cylindrical coordinate system.

Since the calculation results are just a simulation and not real, a numerical model should be validated by comparing the experimental results. the objective of this study is to verify our

Copyright© 2014 by the Japan Society for Aeronautical and Space Sciences and ISTS. All rights reserved.

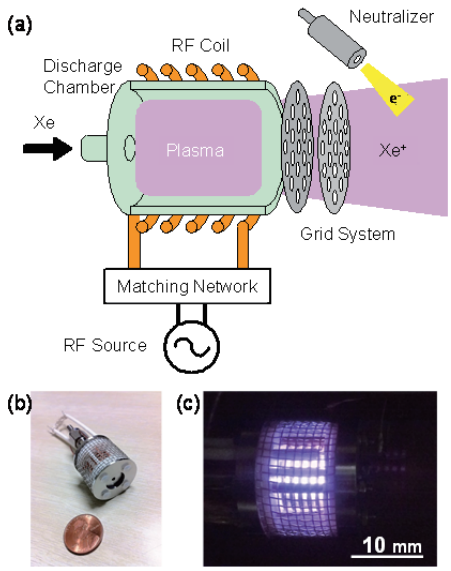

Fig. 1. (a) Schematic of the micro RF ion thruster, and photograph images of (b) the thruster and (c) in Xe plasma-discharging operation.

numerical model so that the model can be used for micro RF ion thruster optimization. In the present study, by using a two-dimensional particle model and a circuit model, which we developed already [2], we investigate the frequency dependence of the microplasma source and the gas flow dependence of ion beam currents. These results are compared with the experimental results for verification of the model. At this stage, the neutralizer is not taken into account in the model; it is left for the future work.

2. Experimental Setup and Procedure

Figure 2(a) shows a cross-sectional view of the micro RF ion thruster. The RF plasma source is made of a quartz tube 10 mm in length, 10 mm in inner diameter, and 12 mm in outer diameter, around which a five-turn copper coil with a diameter of 0.9 mm is wound. A two-grid ion accelerator system is placed at the end of the discharge chamber; the screen grid and the accelerator grid have a single hole of 3.0 and 1.8 mm, respectively, on the central axis. Both the grids are 1.0 mm in thickness with a gap between them of 0.5 mm. The plasma source and the grids are enclosed in a plasma screen biased to the ground potential. All metallic parts including the grids are made of a stainless steel.

Figure 2(b) shows a schematic diagram of the experimental setup. RF signals of 1–500 MHz generated by an oscillator (Agilent Technologies, 8648D) are amplified through a solid state amplifier (THAMWAY, T142-432AA) to powers up to 25 W. A dual directional coupler, RF switch and RF power meter are used to measure the forward and reflected power. The power reported in this paper is the net power supplied to the micro ICP and is determined from the difference in forward and reflected power: $P_{in} = P_{fwd} - P_{ref}$. It should be noted that the ratio of the reflected power to the total power can be less than 1% under most experimental conditions by using the matching network. Working gases of Xe are also supplied to the thruster through a mass flow controller, and a

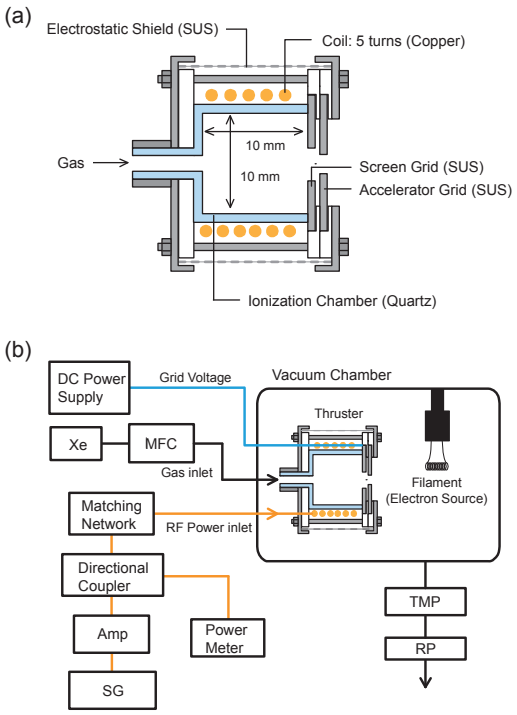

Fig. 2. (a) Cross-sectional view of the micro RF ion thruster, and (b) a schematic diagram of the experimental setup.

filament electron source is employed as a neutralizer. All the experiments are carried out in a stainless-steel vacuum chamber; the chamber is evacuated using a rotary pump and a turbo molecular pump, where the lowest pressure is less than 1×10^{-4} Pa without Xe gas flows. Here, the chamber is used as the ground reference for all experiments.

For electrical diagnostics, a cylindrical Langmuir probe is inserted into the plasma source through the grids hole to determine the electron density thereat. The probe tip is made of a tungsten wire of 0.05 mm in diameter and 1.4 mm in length. The probe measurement is carried out by using a semiconductor parameter analyzer (Hewlett Packard, 4145B) with a low-pass filter to prevent the measurement from the RF interference. It should be noticed that the screen grid is biased to the ground potential, which serves as a reference electrode in the probe circuit when the probe measurement is conducted. A detailed explanation is described elsewhere [3]. Current measurements of the two grids are also conducted for ion beam diagnostics with a shunt resistance of 1 kΩ. The ion beam current I_b is obtained by subtracting the accelerator current from the screen current.

3. Numerical Model

3.1. Particle simulation

Figure 3 shows the simulation areas for the analysis of the micro ICP source and the ion beam extraction. For the analysis of the frequency dependence of microplasma source, only the plasma source is taken into consideration for simplicity. The simulation area is 5 mm in radius and 10 mm in length, and divided at regular intervals with the grid spacing of 0.1 mm. On the other hand, the screen and accelerator grids, and space are also taken into consideration

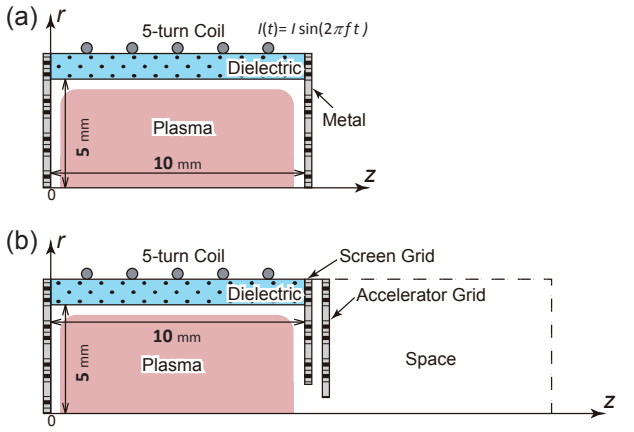

Fig. 3. Simulation areas for the analysis of (a) the micro ICP source and (b) the ion beam extraction.

for the analysis of the ion beam extraction. The length of space area is set at 20 mm downstream of the accelerator grid. The dimensions of the grids are the same as those in the experiment.

To investigate the characteristics of the plasma source, we have conducted two-dimensional axisymmetric particle-in-cell simulations with a Monte Carlo collision algorithm (PIC-MCC). The present PIC-MCC model consists of the electromagnetic equation for the RF-induced azimuthal electric field, the Poisson equation for the electrostatic field due to the space charge, the equation of motion, and collisions of charged particles. A number of simulated superparticles (singly ionized xenon ions and electrons) are loaded into a two-dimensional spatial computational mesh (r, z), along with three velocity components (v_r, v_θ, and v_z). The equation of motion for charged particles is solved explicitly by a time-centered leap frog method for time integration and the Buneman-Boris method for the velocity advance with a coordinate rotation for the position advance. The collision of charged particles can be treated separately from the calculation of motion as long as the time step chosen is much smaller than the mean free time. The postcollision velocities of charged particles are determined by the conservation equations of momentum and energy. The reactions to be taken into account are elastic scattering, excitation, and ionization for electrons [4-6]; and elastic scattering and charge exchange

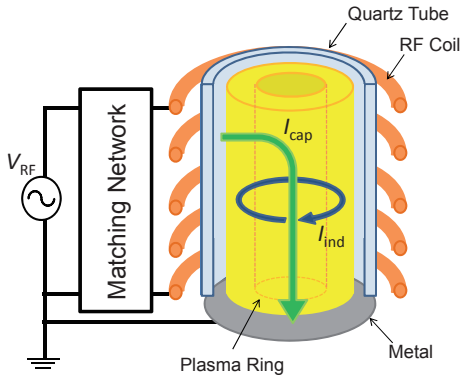

Fig. 4. Schematic of a simplified model of an ICP.

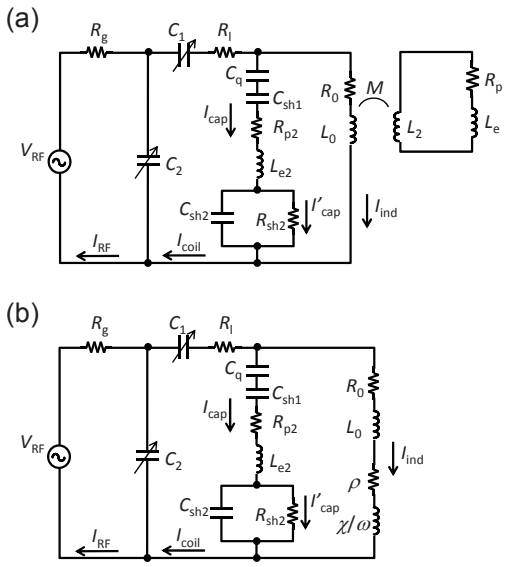

Fig. 5. The transformer circuit with a branch of capacitive coupling and a Γ-shaped matching network. (a) The branch of inductive coupling is modeled as a transformer with the inductive coil taken as the primary circuit and the plasma as the secondary circuit. (b) The secondary circuit transformed into the primary circuit with the plasma impedance $\rho + j\chi$.

for ions [7], which are described by the null-collision method to reduce the calculation time. Neutral particles are assumed to be spatially uniform throughout the simulation with a Maxwellian velocity distribution at a gas temperature of 300 K. The motion of excited-state atoms, Coulomb collisions between charged particles and the secondary electrons are not considered in the present study.

Since a high frequency (> 100 MHz) operation is also calculated, the effect of capacitive coupling of the RF antenna coil is taken into account. We assume that the different turns of the coil act like electrodes in capacitive discharge to include the effect of capacitive coupling. The voltage applied to these electrodes decreases linearly from the powered end of the coil (z = 9 mm) towards the grounded end (z = 1 mm). The powered end of coil oscillates as $\phi(t) = 2\pi L I_{coil} \cos(\omega t)$ when the time-varying current of the RF coil is taken as $I(t) = I_{coil} \sin(\omega t)$. The details of our PIC-MCC model are described in the previous papers and the references therein [8, 9].

3.2. Circuit analysis

Figure 4 shows a schematic of a simplified model of an ICP source with a helical external coil, indicating two current branches: an inductive current I_{ind} and a capacitive current I_{cap}. In this work, the capacitive coupling is also taken into account in the circuit model to investigate the effect of the capacitive coupling on the inductive discharges. The inductive current I_{ind} is assumed to flow azimuthally along a concentric plasma ring (H-mode), whereas the capacitive current I_{cap} flows from a high voltage coil to a ground electrode through the quartz glass, cylindrical plasma, and sheaths (E-mode). In the present case, the same voltage is assumed to be applied through both the paths.

In order to analyze the electrical properties of an inductive RF discharge, it is convenient to represent the inductive discharge with a capacitive coupling by the equivalent circuit

as show in Fig. 5(a). The primary coil of the transformer is the induction coil, which is composed of five turns with inductance L_0 and resistance R_0 [10]. The plasma is assumed to be a one-turn secondary winding of an air-core induction coil with inductance $L_2 + L_e$ and resistance R_p. The plasma inductance consists of two components, the geometrical inductance L_2 due to the plasma current path, and the electron inertia inductance L_e. The amount of inductive coupling between the primary coil and the secondary plasma coil is measured by their mutual inductance M, where $M = k_M\sqrt{L_0L_2}$ with the coupling coefficient of k_M. The transformer circuit can be converted into the one line equivalent circuit as shown in Fig. 5(b). Capacitive coupling is modeled by a series combination of the coil-to-plasma quartz glass capacitance C_q, the sheath capacitance C_{sh1}, the plasma resistance R_{p2} due to ohmic heating of the discharge electrons, the electron inertia inductance L_{e2}, a parallel combination of the plasma-to-ground electrode sheath capacitance C_{sh2}, and the effective sheath resistance R_{sh2} due to a collisionless stochastic process [11]. Here, the RF generator has a typical wave-form of $V_{RF} = V_0 \sin(\omega t)$ with internal resistance R_g. In our study, a Γ-shaped matching network is employed with two variable capacitances of C_1 and C_2. These expressions for the circuit elements are described in our previous paper [2]. It should be noted that the inductive and capacitive power absorptions are defined as $P_{ind} = \rho I_{ind}^2$ and $P_{cap} = R_{p2}I_{cap}^2 + R_{sh}I'^2_{cap}$, respectively, by using the root mean square of the current. The power which is note absorbed by the plasma is deposited into the resistances of the coil and the other transmission lines: $R_0I_{ind}^2 + R_l(I_{ind} + I_{cap})^2$.

4. Results and Discussion

The circuit element analysis was conducted for the wide range of frequency f = 2–500 MHz and pressure p = 1.3–6.3 mTorr (i.e., ν_{me} = 1.0–5.0×10^7 s^{-1} for Xe) at the fixed electron density of 3.0×10^{16} m^{-3}, where the electron density was volume averaged value and it was determined from the PIC calculations. It should be noted that the volume averaged electron density is almost independent of the RF frequency at fixed absorbed power of electrons. Here, the coupling coefficient k_M was set to be 0.2 on the basis of the available experimental study [12].

Figures 6(a) and 6(b) show the inductive and capacitive power absorptions as a function of RF frequency. As shown in the figures, the inductive component of the absorbed power P_{ind} dominates over the rest of components P_{cap} below 10 MHz while the capacitive component dominates over the inductive one over 20 MHz. This is because that the inductive current I_{ind} significantly increases with decreasing RF frequency as shown in Fig. 6(c). On the other hand, the capacitive current I_{cap} increases with increasing RF frequency and then levels off. The capacitive current becomes larger than the inductive current over 100 MHz. Figure 6(d) shows the total power of the RF generator P_g required to deposit 100 mW into the plasma as a function of RF frequency. The RF power P_g significantly increases with decreasing frequency because the larger current at low frequencies leads to a large power loss to the resistances of the coil R_0 and the other transmission lines R_l. As the frequency increases, almost all of the RF power is deposited into the plasma, and then P_g slightly increases because of the increase in resistance (the resistances of R_0 and R_l are proportional to the square root of the RF frequency). It should be noted that P_{ind} and I_{ind} become minimal at the frequency of 200 MHz because the frequency approaches the resonant frequency of the parallel LC circuit shown in Fig. 5.

Figure 7 shows the minimum RF input power P_{in} to sustain

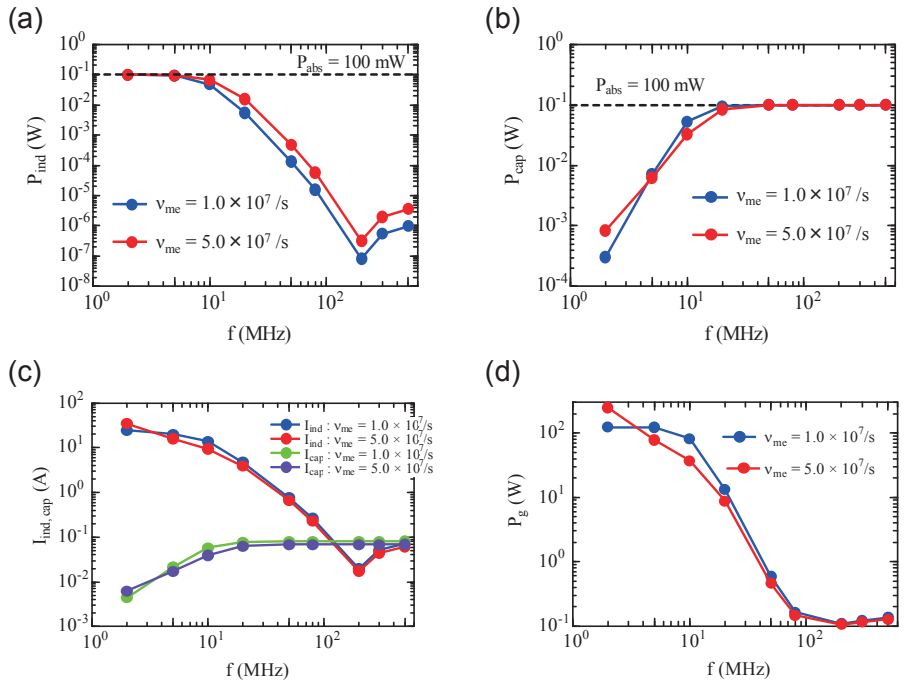

Fig. 6. (a) Inductive and (b) capacitive components of the absorbed power, (c) inductive and capacitive coil currents, and (d) total RF generator power as a function of RF frequency for different electron collision frequencies of 1.0 and 5.0×10^7 s^{-1}.

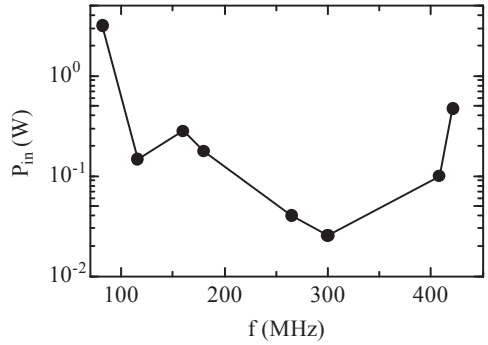

Fig. 7. Minimal RF input power to sustain the plasma discharge as a function of RF frequency.

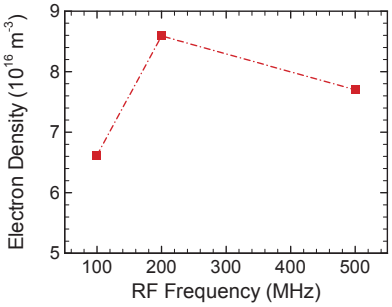

Fig. 9. Electron density as a function of RF frequency, calculated at the Xe gas pressure of 5 mTorr.

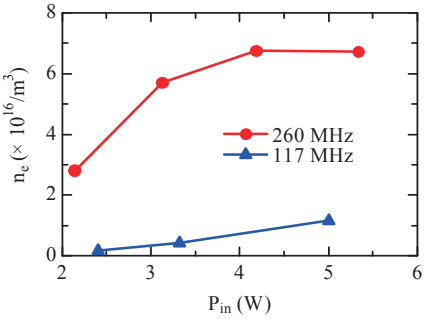

Fig. 8. Electron density as a function of RF input power at the Xe gas flow rate of 2.0 μg/s (0.2 sccm) for the RF frequencies of 117 and 260 MHz.

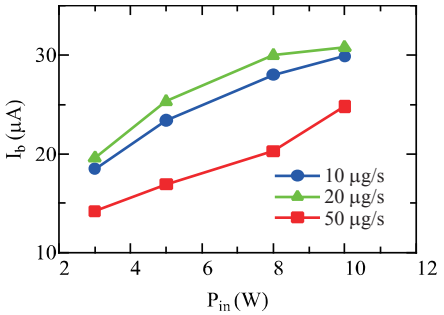

Fig. 10. Ion beam currents as a function of RF input power at f = 160 MHz for different Xe gas flow rates of 10, 20, and 50 μg/s, where the screen and accelerator grid voltages were set at 1050 V and –200 V, respectively.

the plasma discharge as a function of RF frequency in the experiment. The minimum P_{in} decreases with increasing frequency, and then becomes minimal at the frequency of 300 MHz. The minimum P_{in} again increases with increasing frequency over 300 MHz. This tendency is qualitatively in good agreement with the result of the circuit analysis as shown in Fig. 6(d). It should be noted that as the frequency further decreases, the minimum P_{in} increases significantly (not shown here), and at least 10 W was required to sustain the plasma discharge at around f = 10 MHz. This result also implies that a higher RF power is required to sustain the plasma at low frequency because of the high coil current required as shown in Fig. 6(c).

Figure 8 shows the electron density as a function of RF input power measured at the Xe gas flow rate of 2.0 μg/s (0.02 sccm) for the RF frequencies of 117 and 260 MHz. Here, the measurement was conducted three times under each condition, and the only averaged values are plotted in the figure. The electron density increases with increasing RF input power. The electron density at f = 260 MHz is larger than that at f = 117 MHz under all RF power conditions. As indicated in Fig. 2(b), RF input power was measured before the matching network, so that input power includes the power loss to the resistances of the coil and the other transmission lines. The loss at f = 260 MHz is probably lower than that at f = 117 MHz and thus more RF power is deposited into the plasma. This tendency is also confirmed in the PIC simulation result as shown in Fig. 9, where the power absorbed in the plasma is fixed at every RF frequency. In our previous paper [8], PIC calculations showed that at lower frequencies more electrons reach the dielectric window during the positive cycle of the potential oscillation, so that the dielectric window is more negatively charged, which results in the negative potential on the dielectric. This large potential difference between in the bulk and on the dielectric leads to the large ion heating. Since a larger fraction of RF power deposits into ions through the acceleration in the sheath, which reduces the power deposition into electrons, the electron density decreases with decreasing frequency. In addition to the power loss to the resistances of the coil and transmission lines, the effect mentioned above would also cause the large differences in the electron density between 260 MHz and 117 MHz. However, the physical mechanism causing the differences is still unclear and will be discussed in future work.

Figure 10 shows the ion beam currents I_b as a function of RF input power P_{in} measured at f = 160 MHz for different Xe gas flow rates of 10, 20, and 50 μg/s, where the screen and accelerator grid voltages were set at 1050 V and –200 V, respectively. It should be note that when the voltages were applied to the grids, the plasma discharge tended to be unstable and then H-mode discharges were not obtained. The I_b values were taken under the E-mode discharge condition. Moreover, the measurement was carried out three times under each condition, and the only averaged values are plotted in the figure. As shown in the figure, the beam currents increase with increasing RF input power because of the increase in

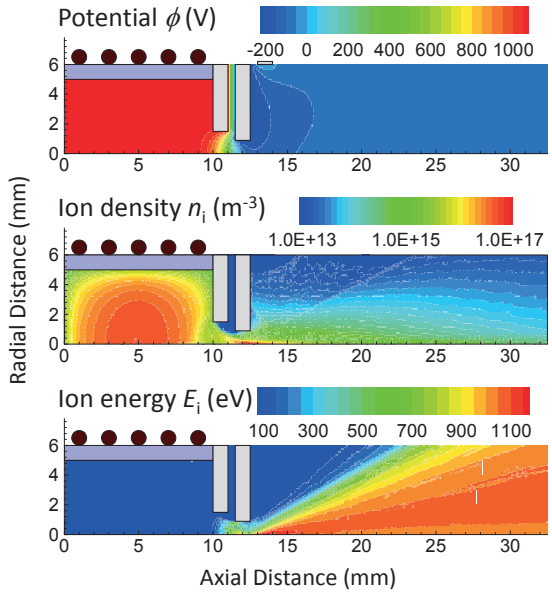

Fig. 11. Two-dimensional distributions of the time-averaged potential ϕ, ion density n_i, and ion energy E_i.

Table. 1. The beam current calculated as a function of Xe gas flow rate.

Xe gas flow rate (μg/s)	I_b (μA)
10	32.1
20	29.9
50	23.8

plasma density as shown in Fig. 8. Although the beam current at 10 μg/s is almost equal to that at 20 μg/s, the beam current of 50 μg/s decreases significantly. The beam currents show low values because the grids have only a single hole. If the H-mode discharge was obtained, the beam current would increase at least more than double.

The calculation of ion beam extraction was also carried out. Figure 11 shows the distributions of the potential, ion density, and ion beam energy at the gas flow rate of 20 μg/s. Note that only the ion density is expressed as logarithmic scale. Most ion beam trajectories seem to fit the single hole on the central axis, but some ions are found to collide with the accelerator grid. Table 1 summarizes the beam currents for different gas flow rates taken from the calculation. As the flow rate increases, the accelerator current increases because of the increase in collisions between ions and neutrals, and thus the beam current is the lowest at the gas flow rate of 50 μg/s. This tendency is consistent with the experimental result.

5. Conclusions

In this work, we have conducted PIC-MCC simulations, external circuit analysis, and measurements of plasma densities and ion beam currents to investigate plasma characteristics and ion beam extraction for a micro RF ion thruster and to validate our numerical model. The numerical results have indicated that relatively high RF frequencies (> 100 MHz) lead to a high coupling efficiency between the RF power and the plasma at low RF powers. However, too high RF frequencies (> 300 MHz) degrade the efficiency. This tendency is qualitatively in good agreement with the experimental results at low RF powers. Moreover, the optimum gas flow rate for ion beam extraction was determined to be 10–20 μg/s in experiments, and this result was also consistent with the numerical result. These comparisons validate our numerical model, and thus the model would be useful to estimate the performance of the micro RF ion thruster. As a next step, the neutralizer will be incorporated into our model to investigate the interaction between ion beams and electron beams.

Acknowledgments

This work was financially supported in part by a Grant-in-Aid for Young Scientists (B) (Grant No. 23760769) from the Japan Society for the Promotion of Science.

References

1) Micci, M. M. and Ketsdever, A. D.: *Micropropulsion for Small Spacecraft*, American Institute of Aeronautics and Astronautics, Reston, 2000.
2) Takao, Y., Eriguchi, K. and Ono, K.: Miniature Ion Thruster Using a Cylindrical Micro ICP, Proceedings of the 48th AIAA/ASME/SAE/ASEE Joint Propulsion Conference & Exhibit, Atlanta, Georgia, USA, 2012, AIAA-2012-3950.
3) Minayeva, O. B. and Hopwood, J.: Langmuir probe diagnostics of a microfabricated inductively coupled plasma on a chip, *J. Appl. Phys.,* **94** (2003), pp. 2821-2828.
4) Hayashi, M.: Determination of electron-xenon total excitation cross-sections, from threshold to 100 eV, from experimental values of Townsend's α, *J. Phys. D,* **16** (1983), pp. 581-589.
5) Heer, F. J. d., Jansen, R. H. J. and Kaay, W. v. d.: Total cross sections for electron scattering by Ne, Ar, Kr and Xe, *J. Phys. B,* **12** (1979), pp. 979-1002.
6) Rapp, D. and Englander-Golden, P.: Total Cross Sections for Ionization and Attachment in Gases by Electron Impact. I. Positive Ionization, *J. Chem. Phys.,* **43** (1965), pp. 1464-1479.
7) Boyd, I. D.: Modeling of the near field plume of a Hall thruster, *J. Appl. Phys.,* **95** (2004), pp. 4575-4584.
8) Takao, Y., Eriguchi, K. and Ono, K.: Effect of capacitive coupling in a miniature inductively coupled plasma source, *J. Appl. Phys.,* **112** (2012), pp. 093306-1-10.
9) Takao, Y., Kusaba, N., Eriguchi, K. and Ono, K.: Two-dimensional particle-in-cell Monte Carlo simulation of a miniature inductively coupled plasma source, *J. Appl. Phys.,* **108** (2010), pp. 093309-1-8.
10) Gudmundsson, J. T. and Lieberman, M. A.: Magnetic induction and plasma impedance in a cylindrical inductive discharge, *Plasma Sources Sci. Technol.,* **6** (1997), pp. 540-550.
11) Yoshiki, H.: Equivalent Circuit Model of an Inductive RF Discharge with a Helical External Coil, *Jpn. J. Appl. Phys.,* **39** (2000), pp. 598-601.
12) Iza, F. and Hopwood, J.: Influence of operating frequency and coupling coefficient on the efficiency of microfabricated inductively coupled plasma sources, *Plasma Sources Sci. Technol.,* **11** (2002), pp. 229-235.